

TCD

8, 805–844, 2014

Sea ice melt pond fraction estimation –  
Part 1

R. K. Scharien et al.

# Sea ice melt pond fraction estimation from dual-polarisation C-band SAR – Part 1: In situ observations

R. K. Scharien, J. Landy, and D. G. Barber

Centre for Earth Observation Science, Faculty of Environment Earth and Resources,  
University of Manitoba, Winnipeg, Manitoba, USA

Received: 19 December 2013 – Accepted: 6 January 2014 – Published: 27 January 2014

Correspondence to: R. K. Scharien (randall.scharien@umanitoba.ca)

Published by Copernicus Publications on behalf of the European Geosciences Union.

Title Page

Abstract

Introduction

Conclusions

References

Tables

Figures

⏪

⏩

◀

▶

Back

Close

Full Screen / Esc

Printer-friendly Version

Interactive Discussion



## Abstract

An understanding of the evolution of melt ponds on Arctic sea ice is important for climate model parameterizations, weather forecast models, and process studies involving mass, energy and biogeochemical exchanges across the ocean-sea ice-atmosphere interface. A field campaign was conducted on landfast first-year sea ice in the Canadian Arctic Archipelago during the summer of 2012, to examine the potential for estimating melt pond fraction from C-band synthetic aperture radar (SAR). In this study, in situ dual-polarisation radar scatterometer observations of pond covered ice are combined with surface physical measurements to analyse the effects of radar and surface parameters on backscatter. LiDAR measurements of ice surface roughness and ultrasonic wind-wave height profiles of melt ponds are used to quantify the sea ice surface rms-height. Variables contributing to the roughness of wind-generated melt pond surface waves within the fetch-limited pond environment are evaluated, and we show that pond roughness and backscatter cannot be explained by wind speed alone. The utility of the VV/HH polarisation ratio (PR) for retrieving melt pond properties including pond fraction, due to the dielectric contrast between free surface water and sea ice, is demonstrated and explained using Bragg scattering theory. Finally, the PR approach is discussed in the context of retrievals from satellite C-, L-, and P-band dual-polarisation SAR.

## 1 Introduction

A recent shift from predominantly thicker, older, multiyear (MY) sea ice to thinner, smoother, seasonal first-year (FY) ice has occurred in response to atmospheric and oceanic warming in the Arctic (Perovich et al., 2007; Kwok et al., 2009). With this change has come an increasing presence of melt ponds on the ice during spring and summer, as a relative lack of topography on FY compared to MY ice promotes the spreading of ponds over a greater area (Eicken et al., 2004). Melt ponds have a con-

TCD

8, 805–844, 2014

## Sea ice melt pond fraction estimation – Part 1

R. K. Scharien et al.

Title Page

Abstract

Introduction

Conclusions

References

Tables

Figures

◀

▶

◀

▶

Back

Close

Full Screen / Esc

Printer-friendly Version

Interactive Discussion



siderably lower albedo than bare sea ice, enhancing melt at the ice surface and within the ice interior, stimulating positive feedback between pond coverage and melt (Morasutti et al., 1996; Hanesiak et al., 2001; Perovich et al., 2003; Holland et al., 2012). Understanding the processes and feedbacks associated with melt pond formation and evolution has become the subject of much interest within a multidisciplinary context.

Regional and basin scale quantification of sea ice melt pond properties first requires improvements to satellite retrievals (IGOS, 2007). With the exception of the highest resolution optical sensors, a sensor footprint contains varying fractions of sea ice, melt ponds, and possibly open water, and each of these surface types exhibits spectral diversity. Thresholding, spectral unmixing, principal components analysis, and artificial neural network approaches have been applied to optical data from Landsat 7 and MODIS scenes to derive estimates of pond fraction (Markus et al., 2003; Tschudi et al., 2008; Rösel and Kaleschke, 2011; Rösel et al., 2012). The latter approach was applied to the MODIS data record for years 2000–2011, enabling the study of anomalies in basin-wide pond fractions over that period (Rösel and Kaleschke, 2012). However, ubiquitous cloud cover over the Arctic during summer prevents the application of this approach on time scales commensurate with intra-seasonal pond fraction variations. Efforts to minimize algorithm errors caused by variations in pond spectral reflection are also on-going (Zege et al., 2012). Satellite passive microwave radiometer and active scatterometer data, acquired independently of cloud cover, have shown promise for identifying seasonal transitions associated with pond formation and drainage (Belchansky et al., 2005; Howell et al., 2006). Their utility lie in the sensitivity of emission or backscatter signals to the occurrence of free water on the ice surface (Hallikainen and Winebrenner, 1992). Unfortunately detection algorithms are limited by coarse (km-scale) spatial resolutions, so that signal confusion is caused by the opening of leads and polynyas due to summer melt and divergent ice motion (Heygster et al., 2012).

Satellite synthetic aperture radar (SAR) is an all-weather, active, microwave remote sensing tool with an established legacy of high spatial resolution (metre-scale) observations of sea ice. Satellite SARs ERS-1/2, RADARSAT-1/2, and ENVISAT-ASAR

TCD

8, 805–844, 2014

## Sea ice melt pond fraction estimation – Part 1

R. K. Scharien et al.

Title Page

Abstract

Introduction

Conclusions

References

Tables

Figures

◀

▶

◀

▶

Back

Close

Full Screen / Esc

Printer-friendly Version

Interactive Discussion



## Sea ice melt pond fraction estimation – Part 1

R. K. Scharien et al.

Title Page

Abstract

Introduction

Conclusions

References

Tables

Figures

◀

▶

◀

▶

Back

Close

Full Screen / Esc

Printer-friendly Version

Interactive Discussion



have provided C-band frequency radar data since 1991 that have been used for regional scale studies and operational observations of ice types, dynamics, and thermodynamic evolution. A categorization of sea ice thermodynamic and SAR backscatter regimes, driven by the seasonality of Arctic solar insolation, have been well defined for single-polarisation C-band SAR (Livingstone et al., 1987; Barber et al., 1995; Yackel et al., 2007). They are denoted fall *freeze-up*, winter, spring *early melt*, *melt onset*, and summer *advanced melt*, with the latter characterised by a persistent above freezing air temperature, an isothermal and decaying ice cover, and the presence of melt ponds. Previous work has shown that the heterogeneous and fluctuating mixture of ice and ponds, combined with variable wind-wave roughness on pond surfaces, results in dynamic variations in single-polarisation backscatter intensities which limit retrievals (Barber and Yackel, 1999; Yackel et al., 2000). In a previous study of the in situ C-band polarimetric backscatter of ponds and ice, Scharien et al. (2012) demonstrated the potential of the co-polarisation ratio, the ratio of linear backscatter channels (VV/HH), for the unambiguous identification of ponds on FY ice. The ratio was much higher for ponds relative to FY ice, provided the ponds were in liquid form (not capped by an ice lid) and the incidence angle was greater than approximately  $35^\circ$ . Scharien et al. (2012) concluded that the ratio be further examined for its utility in subscale pond fraction retrievals from C-band SAR pixels containing horizontally distributed mixture of ponds and ice.

The co-polarisation ratio, hereafter abbreviated PR following the ocean wave literature (Zhang et al., 2011), is measurable using dual-polarised or polarimetric radars. For surface scattering materials which conform to the frequency-dependent smooth surface limit defined by the Bragg or Small Perturbation Model, the PR is independent of surface roughness, and increases with incidence angle at a rate determined by the complex permittivity  $\epsilon^*$  (Fung, 1994; Hajsek et al., 2003). This limit, hereafter termed the Bragg limit, is defined as  $ks < 0.3$ , where  $k$  is the radar wavenumber and  $s$  the surface rms-height. When either the smooth surface limit is exceeded, or non-Bragg scattering processes such as volume scattering are present in the backscattered sig-

nal, the polarisation diversity between VV and HH channels is damped. This damping causes the PR at a given incidence angle to tend towards unity, with stronger damping linked to increasing surface roughness or non-Bragg scattering effects.

In practice the Bragg model is an approximate solution that is also limited in its direct application to natural surfaces by the validity criterion (Hajnsek et al., 2003). Most natural surfaces fall above the roughness imposed limit of the model. Empirical and semiempirical models have extended the Bragg model to include a wider range of roughness conditions and specific cover types, with the most advanced application the inversion of the volumetric moisture content of bare soils (Oh et al., 1992; Dubois et al., 1995). Recently, polarimetric amplitude and phase information has been used to account for secondary scattering effects, e.g. from stalks, and to decouple scattering mechanisms in soil moisture applications. This has led to more robust retrievals including estimations in the presence of vegetation cover (see, e.g. Hajnsek et al., 2003; Jagdhuber et al., 2012 and references therein).

For sea ice, studies of the C-band PR from the airborne and satellite SAR imagery have demonstrated its utility for separating FY and MY ice types from young ice, leads, and open water during the winter season (Thomsen et al., 1998; Scheuchl et al., 2004; Nghiem and Bertoia, 2001; Geldsetzer and Yackel, 2009). Separation is based on the higher PR from saline young ice and free water in leads and ocean compared to mature ice due to higher relative permittivity. For mature ice types, morphological changes contribute to multiple scattering at the surface due to enhanced roughness relative to radar wavelength, and bulk desalination contributes to enhanced radar penetration and multiple (volume) scattering from within the ice. Both of these effects lead to convergence between HH and VV. Correlations between sea ice thickness and bulk salinity has facilitated the use of C-band PR for proxy thickness estimates (Zabel et al., 1996; Nakamura et al., 2009). Other applications of C-band PR models have included wind speed retrievals from open ocean (e.g. Vachon and Wolfe, 2011; Zhang et al., 2011). Combined with empirical geophysical model functions developed for retrievals of wind vector data from VV backscatter, PR models enable the use of single-polarisation HH

Sea ice melt pond fraction estimation – Part 1

R. K. Scharien et al.

Title Page

Abstract Introduction

Conclusions References

Tables Figures

◀ ▶

◀ ▶

Back Close

Full Screen / Esc

Printer-friendly Version

Interactive Discussion



data for accurate wind retrievals by facilitating the conversion of HH to estimates of VV (Horstmann et al., 2000). Recently, PR approaches have been assessed for their utility in resolving dielectric mixtures such as oil slicks on the ocean surface (Minchew et al., 2012) and within a sea ice environment (Brekke, 2013).

In June 2012, a study dedicated to understanding the multiscale, C-band frequency, polarimetric backscatter of FY ice during the advanced melt period was conducted in the central Canadian Arctic Archipelago. In situ polarimetric backscatter and morphological measurements of melt pond covered FY ice were combined with aerial surveys of melt pond fraction and RADARSAT-2 satellite observations of polarimetric backscatter. Despite the collection of experimental polarimetric data, focus is placed on utility of dual-polarisation rather than polarimetric SAR data for wide-swath melt pond information retrievals, as polarimetric data are presently limited to very narrow swath widths ( $\leq 50$  km). Furthermore, our working hypothesis states that the timing of sea ice pond formation and the evolution of pond fraction are retrievable from PR measured at C-band frequency on the basis of Bragg scattering theory. In this paper (Part 1), the following research questions regarding the in situ scale are addressed: (1) do bare ice and melt ponds conform to the frequency-dependent surface roughness criterion of the Bragg scattering model? And (2) what are the limiting radar and target parameters on the unambiguous retrieval of melt pond information from dual-polarisation SAR? The first question explicitly addresses the PR in the context of Bragg scattering, while the second question also considers PR along with the cross-polarisation ratio (HV/HH, abbreviated  $PR_x$ ) as potential pond information sources.

An overview of the radar and surface parameters affecting microwave scattering from sea ice during advanced melt is given in Sect. 2. A description of the study area and methods for data collection and analysis is provided in Sect. 3, followed by results in Sect. 4. Significant discussion points focusing on the PR behaviour of the individual, sub pixel-scale, surface types comprising a typical SAR resolution cell are summarized in Sect. 5. Our conclusions, in Sect. 6, provide the basis for a companion paper (Part

---

## Sea ice melt pond fraction estimation – Part 1

R. K. Scharien et al.

---

[Title Page](#)[Abstract](#)[Introduction](#)[Conclusions](#)[References](#)[Tables](#)[Figures](#)[⏪](#)[⏩](#)[◀](#)[▶](#)[Back](#)[Close](#)[Full Screen / Esc](#)[Printer-friendly Version](#)[Interactive Discussion](#)

2), which provides an assessment of application approaches for PR based mapping of FY ice pond fraction using calibrated RADARSAT-2 SAR data.

## 2 Physical model

An ensemble of radar and target parameters contribute to linear polarisation backscatter magnitudes from sea ice during advanced melt or ponding period (Fig. 1). In this study, the radar parameters are determined by the in situ scatterometer, described in Sect. 3.2. Our study is limited to the C-band frequency ( $5.5 \text{ GHz} \pm 250 \text{ MHz}$ ), though in the discussion section the behaviour of other frequencies (P- and L-band) is considered in relation to measured surface roughness. Polarisation parameters under consideration include ratios PR and  $\text{PR}_x$ , with linear channel (VV, HH, and HV) intensities included where relevant. Incidence angles across a range typical of contemporary satellite SAR are considered ( $20\text{--}60^\circ$ ). Based on the Bragg model, larger incidence angles are expected to enhance pond discrimination on the basis of the permittivity contrast between free water and ice. The main problem regarding incidence angle is defining the range over which the permittivity contrast yields a detectable separation between pond and ice.

The role of radar azimuth, the angle of the incident radar illumination relative to the orientation of wind-waves, on backscatter is yet uncertain for the pond situation. The asymmetry effect, as it is termed in the ocean literature, is well described for backscatter magnitudes from fully developed seas (Ulaby et al., 1986). At fixed incidence angle and polarisation, backscatter is strongest when the radar beam is aligned upwind and perpendicular to the waves ( $\varphi = 0^\circ$ ), weakest in the crosswind orientation and parallel to the waves ( $\varphi = 90^\circ$ ), and otherwise of intermediate magnitudes. The asymmetry effect on single-polarisation backscatter from ponds is expected to be consistent with that of ocean waves, the behaviour of polarisation ratios requires analysis. As per the working hypothesis of this study, independence of the PR from surface roughness implies

TCD

8, 805–844, 2014

### Sea ice melt pond fraction estimation – Part 1

R. K. Scharien et al.

Title Page

Abstract

Introduction

Conclusions

References

Tables

Figures

◀

▶

◀

▶

Back

Close

Full Screen / Esc

Printer-friendly Version

Interactive Discussion



independence from the asymmetry effect. This is desirable from a retrieval perspective, as it means that ancillary wind direction data would not be required for interpretations.

Backscatter is also dependent on variations in surface parameters (Fig. 1) considered relative to the radar parameters. The temperature of a melt pond is close to the triple point of water, as it is in contact with ice, so the net energy balance across the pond surface is generally close to zero (Barber and Yackel, 1999). Minor fluctuations in the energy balance control the phase state of the pond surface, so that a loss of energy from the pond to the atmosphere causes a 1–2 cm ice lid to form over the pond and equally, a loss of energy from the atmosphere to the pond causes the ice lid to melt. Consequently the phase state of the pond surface tends to follow the sun angle and ice lids form overnight (Yackel et al., 2007), or when a sudden clearing of low level stratus cloud cover causes a greater heat loss than input from the sun (Untersteiner, 2004). The phase state of a pond is related to its surface roughness and permittivity. In the melting state, ponds on FY ice are typically metre-scale, relatively shallow (cm-scale), pools of high dielectric water. Single-polarisation backscatter increases in proportion to the boundary layer wind speed, as the roughness of the pond surface spans specular and isotropic scattering regimes. When considered as an ensemble of ponds and ice, several secondary parameters contribute to the pond surface roughness and backscatter (Fig. 1). These include pond fetch, orientation, depth, and connectivity. Orientation describes the shape of a pond relative to the wind direction, with elongated long axes enhancing pond fetch and wind-wave growth. Connectivity refers to channelling between ponds that occurs on FY ice (Eicken et al., 2002) and, though not previously studied, expectedly enhances the transfer of wind-wave energy (less dissipation) between ponds. Of these secondary parameters only pond depth and fetch have been analysed in relation to C-band backscatter, with pond depth found to be a significant explanatory variable, along with wind speed, for changes in single-polarisation backscatter magnitude (Scharien et al., 2012). When ice lids form on a pond, they deter roughness caused by wind stress on free water.

## Sea ice melt pond fraction estimation – Part 1

R. K. Scharien et al.

Title Page

Abstract

Introduction

Conclusions

References

Tables

Figures

⏪

⏩

◀

▶

Back

Close

Full Screen / Esc

Printer-friendly Version

Interactive Discussion



## Sea ice melt pond fraction estimation – Part 1

R. K. Scharien et al.

Title Page

Abstract

Introduction

Conclusions

References

Tables

Figures

◀

▶

◀

▶

Back

Close

Full Screen / Esc

Printer-friendly Version

Interactive Discussion



Bare FY ice adjacent to ponds is a predominantly surface scatterer, with backscatter occurring from the wetted, granular, decaying surface ice crystals. Volume scattering at C-band frequency has been shown to occur, when incident energy penetrates the surface and scattering occurs from within the voids and air bubbles in desalinated upper (cm-scale) layers (Scharien et al., 2010). Notably, Scharien et al. (2010) found no seasonal signal (increase) in volume scattering related to FY ice ablation and desalination in advanced melt FY ice; rather, volume scattering depended on the occurrence of freezing conditions and periods when the moisture content of upper ice layers, driven by localized melt vs. drainage rates, was low.

The model in Fig. 1 does not consider a meteoric snow cover. This is despite the initial pond formation period being characterised by a rapidly melting snow cover, with significant melt water production from snow, and very little percolation into the relatively impermeable ice volume. On FY ice this results in surface flooding to pond fractions typically > 50 %, with the complete decay of the snow cover occurring over a period of no more than one week (Barber and Yackel, 1999; Eicken et al., 2002; Scharien and Yackel, 2005; Polashenski et al., 2012). Though it is probable that permittivity fluctuations due to variations in the volumetric moisture context of melting snow would influence backscatter at this initial stage, we do not consider snow since: (1) our in situ observations were restricted to the period after snow ablation; and (2) Scharien et al. (2012) found that the C-band linear polarisation backscatter and PR levels were similar for snow compared to bare FY ice during the ponding period.

### 3 Methods

#### 3.1 Description of the study area

Data were collected during the Arctic-Ice Covered Ecosystem (Arctic-ICE) field project on seasonal landfast ice in the central CAA, adjacent to the hamlet of Resolute Bay, from May to July 2012 (Fig. 2, top left). Arctic-ICE is an interdisciplinary project with

focus on biogeochemical and physical processes occurring at the ocean-sea ice-atmosphere (OSA) interface during the spring-summer snow melt and melt pond periods. Studies are conducted on landfast FY ice, an undeformed and seasonal ice type which comprises a stable platform from which to conduct collocated time series in situ and remote sensing measurements of sea ice without the ambiguities associated with ice motion. References to ice hereafter refer to this sea ice type, unless otherwise stated.

### 3.2 Data collection

Polarimetric backscatter measurements from elemental surface types bare ice and melt ponds (hereafter “ponds”) were collected at the Arctic-ICE field site using a sled-mounted C-band frequency scatterometer (Cscat) operating at 2.4 m height (Fig. 2, top right). The low noise floor of the system,  $-35$  dB for co-polarised and  $-45$  dB for cross-polarised channels, makes the instrument ideal for studying the polarimetric backscatter behaviour of low intensity targets such as summer sea ice. Cscat radar parameters are provided in Table 1 with standardized calibration and data processing procedures for the instrument found in Geldsetzer et al. (2007). The Cscat was towed by snow-machine, and a computer controlled tracking and positioning system used to isolate homogeneous targets over a small ( $< 10$  m<sup>2</sup>) footprint. A single scan involved the collection of polarimetric scattering data over a set of pre-programmed scan lines defined by specific incidence angles of consistent azimuth widths, based on the local position of the sensor. Scan lines across the  $25$ – $65^\circ$  incidence angle range were collected at  $5^\circ$  increments, with pond data at near range incidence angles ( $25$ – $35^\circ$ ) occasionally discarded due to overlap between the pond and the ice at the pond edge. A  $20^\circ$  azimuth width was used for pond scans, compared to  $40^\circ$  for ice scans, to focus the radar beam relative to wind-waves on pond surfaces. With each pond scan, time-synched wind data was recorded at 1 s resolution and 1 m height using a tripod mounted RM-Young 05103 wind monitor. The sensor was positioned adjacent to the scanned area, close enough to characterise wind without interference from the Cscat.

## Sea ice melt pond fraction estimation – Part 1

R. K. Scharien et al.

Title Page

Abstract

Introduction

Conclusions

References

Tables

Figures

◀

▶

◀

▶

Back

Close

Full Screen / Esc

Printer-friendly Version

Interactive Discussion



## Sea ice melt pond fraction estimation – Part 1

R. K. Scharien et al.

Title Page

Abstract

Introduction

Conclusions

References

Tables

Figures

◀

▶

◀

▶

Back

Close

Full Screen / Esc

Printer-friendly Version

Interactive Discussion



The radar azimuth (asymmetry) effect was considered by restricting Cscat pond scans to upwind (radar azimuth,  $\varphi = 0^\circ$ ) and crosswind ( $\varphi = 90^\circ$ ) configurations. This enabled the acquisition of backscatter intensity extremes in terms of the single-polarisation radar response to wind-waves, and also facilitated a practical sampling strategy within the logistically challenging pond covered sea ice environment. Sensing at  $\varphi = 0^\circ$  was also used as a control for the evaluation of variables contributing to wind-wave amplitude and backscatter, as described in Sect. 2.

A total of 210 Cscat scans were collected between 16 and 24 June. Each scan is comprised of several ( $> 100$ ) independent samples collected as a series of data blocks across a  $20^\circ$  or  $40^\circ$  degree azimuth width. The number of independent samples is dependent on the azimuth width combined with the incidence angle, as the scan line widens at higher incidence angles. For example, the  $20^\circ$  azimuth width resulted in 7 samples collected at the near-range ( $25^\circ$  incidence angle) and 37 at the far-range ( $65^\circ$  incidence angle), with 123 independent samples collected across the  $25$ – $65^\circ$  incidence angle range. An average covariance matrix of the complex scattering amplitudes of all independent samples within a scan line was output, providing robust estimates of the incidence angle dependent complex scattering coefficients of the target for each scan.

Morphological measurements focused on the small scale (radar scale) surface roughness of ice and ponds. A high-resolution terrestrial laser scanning (or LiDAR) system was used to create digital elevation models of snow and ice surface targets coincident to areas scanned by the Cscat from YD 158 (6 June) to YD 177 (25 June). The scanner was mounted on a tripod and configured to acquire several  $3.5 \times 3.5$  m elevation models of the surface at a measurement spacing of  $< 2$  mm. LiDAR models were then resampled to a regular 2 mm grid and detrended using a Fast Fourier Transform (FFT-) based technique to remove large-scale ice topography (Fig. 2, bottom right). Surface roughness parameters rms-height ( $s_r$ ) and correlation length ( $l$ ) were then extracted using a two-dimensional cross-correlation technique outlined in Landy et al. (2013).

## Sea ice melt pond fraction estimation – Part 1

R. K. Scharien et al.

Title Page

Abstract

Introduction

Conclusions

References

Tables

Figures

◀

▶

◀

▶

Back

Close

Full Screen / Esc

Printer-friendly Version

Interactive Discussion



Pond surface wave height profiles were collected as part of a larger study examining air-water interactions. A Senix Corporation ToughSonic type TPSC30S1 ultrasonic distance sensor was mounted to an adjustable, counter-weighted, boom arm extending between 0.5 and 1 m laterally from a tripod placed adjacent to, or within, the a Cscat footprint after the completion of scanning (Fig. 2, top left). 30 s samples of profiles taken at 40 Hz sampling rate, with an estimated sensor spot size of 0.04 m, were sub-sampled by a factor of 5, and the pond surface rms-height ( $s_w$ ) was calculated. During calm conditions a flat pond surface was selected, and repeated measurements made in order to determine the precision of the instrument. These data reveal a positive  $s_w$  bias of 0.0001 m from this method. Additional pond morphological measurements included transects of pond depth recorded at an interval of 0.5 m, fetch lengths, and minor/major axis lengths. The connectivity between ponds was qualitatively assessed using a combination of surface and aerial photographs (Fig. 2, bottom left).

Ancillary data include daily measurements of snow and ice thickness, and vertical profiles of temperature, salinity, and density. Snow volumetric moisture content measurements were made using the impedance probe and inversion method described in Scharien et al. (2010). Though the last snow measurements were made on YD 164, one day prior to advanced melt, they are included to provide context for the evolution of LiDAR surface roughness measurements in Sect. 4.1. Hourly averaged measurements of air temperature (2 m) and wind speed/direction (3 m) are derived from instrumentation mounted to a small micrometeorological tower located on the ice surface, as part of the larger Arctic-ICE field study.

### 3.3 Data analysis

Cscat scans were grouped according to the following classes, with the number of scans in brackets: pond-upwind,  $\varphi = 0^\circ$  (140); pond-crosswind  $\varphi = 90^\circ$  (17); pond-ice lid (4); and bare ice (49). Parameters extracted from scattering matrix data included linear co- and cross-polarisation backscatter coefficients (HH, VV, and HV), with VH discarded due to reciprocity. Backscatter data were then subject to two radiometric quality assur-

ance steps, which are particularly important due to the low intensity nature of summer sea ice. Values at each polarisation state that exceeded the relevant NESZ (Table 1) were passed to a signal-to-noise (SNR) test following the Rose criterion (SNR ≥ 5). Retained data were then used to derive polarimetric ratios.

All wind speed measurements were adjusted to neutral stability values at a reference 10 m height, using a typical aerodynamic roughness length of 0.001 m for summer sea ice (Andreas et al., 2005). Hereafter the symbol  $U_{10}$  is used for all references to the corrected 10 m wind speeds. Data from each Cscat scan was matched to a coincident average  $U_{10}$  and median direction.

As the main focus was on PR and the evaluation of Bragg scattering, a comparison of pond and ice PR measurements to Bragg modelled PR for each feature was made. For a surface within the limiting Bragg criterion, the PR is a ratio of its horizontal and vertical reflection coefficients  $R_{vv}$  and  $R_{hh}$ :

$$R_{vv} = \frac{(\varepsilon_r - 1)\{\sin^2(\theta) - \varepsilon_r[1 + \sin^2(\theta)]\}}{\left(\varepsilon_r \cos(\theta) + \sqrt{\varepsilon_r - \sin^2(\theta)}\right)^2}, \quad (1)$$

$$R_{hh} = \frac{\cos(\theta) - \sqrt{\varepsilon_r - \sin^2(\theta)}}{\cos(\theta) + \sqrt{\varepsilon_r - \sin^2(\theta)}}. \quad (2)$$

Bragg ratio estimates require an incidence angle ( $\theta$ ) and the complex permittivity ( $\varepsilon_r$ ) of the material. We used values of  $\varepsilon_r = 67.03 + 35.96i$  to represent freshwater pond water at 0.5 °C and  $\varepsilon_r = 3.11 + 0.208i$  to represent the advanced melt ice cover (Ulaby et al., 1986). Additionally, empirically derived ocean surface PR models from Vachon and Wolfe (2011) and Zhang et al. (2011) are used for comparison to observed and modelled PR from ponds.

A specific upwind to crosswind ratio experiment, allowing for a controlled evaluation of the effect of radar asymmetry on polarisation ratios, was conducted using Cscat pond

## Sea ice melt pond fraction estimation – Part 1

R. K. Scharien et al.

Title Page

Abstract

Introduction

Conclusions

References

Tables

Figures

◀

▶

◀

▶

Back

Close

Full Screen / Esc

Printer-friendly Version

Interactive Discussion



samples. We chose three cases when replicate pond samples (> 2) were acquired at upwind orientation, followed immediately by replicate samples at crosswind orientation from the same pond. Each case includes a wind-synched pond surface wave amplitude profile of 30 s duration recorded in proximity to the Cscat footprint. From each case, the upwind to crosswind ratio (difference in decibel scale) was calculated:

$$\Delta PR = \overline{PR}_{\phi=90^\circ} - \overline{PR}_{\phi=0^\circ} [\text{dB}], \quad (3)$$

with Eq. (2) also repeated for  $PR_x$  in place of PR.

## 4 Results

### 4.1 Evolution of the sea ice cover

#### 4.1.1 Melt onset

An assessment of conditions during melt onset (MO), beginning YD 158 and up to pond onset (PO) on YD 165, provides context for the interpretation of the time series evolution of ice surface roughness provided later. Beginning YD 158 the air temperature was above 0°C, with the exception of a few brief overnight periods ( $\geq -1.1^\circ\text{C}$ ). Snow thickness was < 0.10 m, and the volume was isothermal and devoid of a saline basal layer which typically forms via upward brine migration from the ice surface during colder periods. The snow was low density (< 200 kg m<sup>-3</sup>) and comprised melt-freeze metamorphosed grains which increased in size with depth. Bulk volumetric moisture content ranged from 3–4%, with an observed slush layer at the snow–ice interface. Basal slush layer re-freezing and the formation of a rough superimposed ice layer with cm-scale undulations was observed for some snow patches, while other patches had a smooth basal layer. On YD 164, immediately prior to PO, the snow cover was reduced to sporadic patches of 0.03 m maximum thickness and remnant rough basal layers. During MO the top 0.10 m of the ice volume became isothermal and its bulk

salinity reduced from 1.7–0.5‰. A storm event, with high winds and rain, coincided with PO, after which no snow and rough basal layer patches remained.

LiDAR measured small scale surface roughness  $s_i$  measurements during the MO and ponding periods are shown in Fig. 3. There is negligible difference in  $s_i$  from melting snow during MO to the exposed ice during ponding. The exceptionally large  $s_i$  (0.0036 m) on YD 161 was derived from a LiDAR map (c.f. Fig. 2) of the rough superimposed basal layer, measured after careful removal of the snow cover (0.0018 m). This is the only case where  $ks$  (0.40) exceeds the Bragg limit. Otherwise the melting snow and exposed ice cover  $s_i$  ranges from 0.0011–0.0020 m, which corresponds to a  $ks$  range of 0.12–0.22, below the Bragg limit. With the exception of rough basal ice patches during MO, the PR at C-band frequency is unaffected by bare ice surface roughness within the limits defined by the Bragg model.

#### 4.1.2 Melt ponds

Pond depths ranged from 0.03–0.08 m throughout the study. Pond depth was not observed to increase with time, and variations appeared to be driven by the balance between melting (melt water supply) and drainage rates at any one time (Eicken et al., 2002). The pond aspect ratio, the ratio of minor and major axis lengths, ranged from 0.2–0.7 with an average of 0.5. The elongated shape of ponds means their orientation relative to wind direction is a factor in wind-wave roughness. Thus, when considering a horizontally distributed mixture of ponds and bare ice, an increase in fetch occurs when the wind direction is parallel to the long axes of ponds. However, the treatment of ponds as discrete elements is cautioned. As illustrated by the aerial photo in Fig. 2, bare ice patches exist as discrete elements situated within a water background. The connected nature of the ponds was qualitatively considered, with less wave energy dissipation (higher waves) observed when the wind direction was aligned with the pathways adjoining ponds. Cscat and pond roughness measurements were made at fetch lengths varying from 7.8–34.8 m.

## Sea ice melt pond fraction estimation – Part 1

R. K. Scharien et al.

Title Page

Abstract

Introduction

Conclusions

References

Tables

Figures



Back

Close

Full Screen / Esc

Printer-friendly Version

Interactive Discussion



## Sea ice melt pond fraction estimation – Part 1

R. K. Scharien et al.

Title Page

Abstract

Introduction

Conclusions

References

Tables

Figures

◀

▶

◀

▶

Back

Close

Full Screen / Esc

Printer-friendly Version

Interactive Discussion



The small-scale surface roughness of ponds  $s_w$  varies from 0.0001, within the detection limit of the instrument, to 0.0070 m and exhibits a power law dependence on  $U_{10}$  over the measured 2.4–11.4  $\text{ms}^{-1}$  range (Fig. 4). The upper limit of  $s_w$  is greater than it is for  $s_i$ , and values in excess of the Bragg limit at C-band frequency are observed, as denoted by the shaded portion in Fig. 4. A  $U_{10}$  threshold of 6.4  $\text{ms}^{-1}$ , beyond which the PR is expected to be dependent on surface roughness, is derived from Fig. 4. However the measurements were noted to have been taken during a period of sustained winds parallel to the pathways interconnecting ponds. A clustering of  $s_w$  values nearer to  $U_{10} \sim 8.0 \text{ms}^{-1}$  suggests that the Bragg limit may tend to a higher  $U_{10}$  threshold. Hourly wind measurements from the micrometeorological tower showed that the  $U_{10}$  was  $\geq 6.4 \text{ms}^{-1}$  20 % of the time during ponding, and  $\geq 8.0 \text{ms}^{-1}$  9 % of the time.

## 4.2 Microwave backscatter from pond-covered sea ice

### 4.2.1 Polarisation ratios

Figure 5 shows the angular response, across the 25–60° incidence angle range, of PR from all Cscat measurements during ponding. A large scatter in the pond data is partly attributed to the sampling strategy. A high density of samples were acquired with  $\varphi = 0^\circ$ , so that the maximum sensitivity of backscatter to wind-waves, including waves beyond the Bragg limit, could be evaluated against the working hypothesis. These samples were acquired over a coincident  $U_{10}$  range of 0.9–10.0  $\text{ms}^{-1}$ .

A model was fit to all of the Cscat pond observations and appears as the “Model” line in Fig. 5. It takes the form of a quadratic:

$$\text{PR} = A + B\theta + C\theta^2, \quad (4)$$

where  $\theta$  is the incidence angle and coefficients A–C are given in Table 2. The incidence angle dependence of pond PR and separation from ice at higher incidence angles is consistent with Bragg scattering. However, observed pond PR is consistently lower

## Sea ice melt pond fraction estimation – Part 1

R. K. Scharien et al.

Title Page

Abstract

Introduction

Conclusions

References

Tables

Figures

⏪

⏩

◀

▶

Back

Close

Full Screen / Esc

Printer-friendly Version

Interactive Discussion



than the Bragg model prediction (the “Bragg” line in Fig. 5). We found that varying the assumed permittivity of water in the Bragg model had a minimal effect on modelled PR (not shown), which suggests the offset in Fig. 5 is due to other factors. The first factor is non-Bragg scattering from wind-waves which exceed the Bragg limit, consistent with reductions in PR relative to Bragg estimates. However, even PR measurements from very calm conditions evidently fall below the Bragg model estimate. A second factor, as proposed by Thompson et al. (1998), is a deficiency in the Bragg scattering model. It is generally understood that the Bragg model does not correctly account for large scale wave features on an ocean surface, as these waves are rougher than the Bragg limit. A two-scale or composite modelling approach attempts to account for this by dividing the surface wave spectrum into short and long waves, with the former propagating on the latter (Plant, 1990). As Thompson et al. (1998) found, composite-type model estimates of the HH polarisation are still lower than observed, leading to higher Bragg-based PR estimates compared to measurements. They suggest an empirical fit to observed PR data as being more robust. Two such ocean models, empirically derived from RADARSAT-2 observations, are also shown in Fig. 5.

Modelled ocean PR in Fig. 5 departs further from Bragg PR than does the pond model, particularly at incidence angles above  $\sim 40^\circ$ . The departure of the ocean models from the Bragg model appears to be the result of a combination of large-scale wave effects and the deficiency of the Bragg model. The pond PR model, which does not include large-scale wave effects, still departs from the Bragg estimate, which provides evidence in support of the Bragg model deficiency claim.

The PR from ice is also below Bragg model based ice PR predictions (not shown in Fig. 5). Using the assumed permittivity of  $3.11 + 0.208i$ , modelled ice PR are about 2–3 dB higher. As was the case for ponds, we also found that varying the assumed dielectric constant had little effect on modelled PR. Instead of showing a Bragg-like dependence on incidence angle, the observed PR remains close to null across the full  $25\text{--}60^\circ$  range. This behaviour is consistent with the presence of non-Bragg volume scattering in the desalinated upper layer of the ice. As outlined in the introduction,

volume scattering from the desalinated upper layers of FY ice adjacent to ponds is known to occur (Scharien et al., 2010). The scatter of data points at any incidence angle is expected from a mixture of surface (Bragg) and volume scattering mechanisms observed at different times throughout the study.

Other observations from Fig. 5 include measured PR from ponds which are covered by an ice lid. Ice lid PR overlaps with bare ice, which indicates that the PR cannot be used to discriminate ponds in this case. PR observations of ponds are also distinguished by radar azimuth, with data points corresponding to  $\varphi = 0^\circ$  and  $\varphi = 90^\circ$ . The effect of  $\varphi$  on PR is not readily apparent within the scatter of points in the Fig. 5. The role of  $\varphi$  is addressed in detail in Sect. 3.2.3.

Figure 6 shows the angular response, across a  $25\text{--}60^\circ$  incidence angle range, of  $PR_x$  from all Cscat measurements during the ponding period. Only generalisations regarding the scattering behaviour of features can be made. A large scatter in the pond data can be attributed to the influence of surface scattering from wind-waves, which is expected to be greater for HH relative to HV due to the absence of depolarisation effects. Larger pond  $PR_x$  at high incidence angles (greater than  $50^\circ$ ) is observed when  $\varphi = 90^\circ$  rather than when  $\varphi = 0$ . As observed for PR, there is a negligible trend in  $PR_x$  with increasing incidence angle for the ice. The role of  $\varphi$  on  $PR_x$  is addressed in Sect. 3.2.3.

#### 4.2.2 Wind speed

Linear polarisation VV, HH, and HV backscatter magnitudes at  $10^\circ$  incidence angle intervals are shown as functions of  $U_{10}$  in Fig. 7. Only samples taken with  $\varphi = 0^\circ$  are given. These data are essential for providing insights into the individual parameters comprising the polarisation ratios. Allowing for variations in surface roughness caused by pond fetch, shape, and depth, a  $U_{10} \sim 3\text{ ms}^{-1}$  is required before wind-waves on pond surfaces are large enough to cause backscatter. This threshold is consistent with that determined for C-band backscatter from an ocean surface at  $0^\circ\text{C}$  (Donelan and Pierson, 1987). The increase in backscatter which occurs at the threshold point is con-

TCD

8, 805–844, 2014

## Sea ice melt pond fraction estimation – Part 1

R. K. Scharien et al.

Title Page

Abstract

Introduction

Conclusions

References

Tables

Figures

◀

▶

◀

▶

Back

Close

Full Screen / Esc

Printer-friendly Version

Interactive Discussion



5 siderable in magnitude, particularly at small incidence angles where it is 20 and 30 dB for HH and VV, respectively. At incidence angles greater than  $25^\circ$ , polarisation diversity consistent with Bragg scattering becomes apparent. Separation between VV and HH occurs as HH maxima are less than VV, particularly at larger (grazing) incidence angles. Convergence between VV and HH channels, analogous to a reduction in PR, is evident at higher  $U_{10}$  and for moderate to large incidence angles. HV in Fig. 7 is very low and variability due to  $U_{10}$  at incidence angles greater than  $25^\circ$  are unlikely to be detectable by contemporary satellite SARs.

10 Pond PR (top) and  $PR_x$  (bottom) at  $10^\circ$  incidence angle intervals and  $\varphi = 0^\circ$  configuration are shown as functions of  $U_{10}$  in Fig. 8. The PR is inversely related to  $U_{10}$  and, above the  $3 \text{ ms}^{-1}$  threshold, varies by as much as 5–8 dB depending on the incidence angle. Referring back to Fig. 7, the negative trend in PR in Fig. 8 is due to the greater relative sensitivity of HH to  $U_{10}$ . Below the  $3 \text{ ms}^{-1}$  threshold the behaviour of PR is not consistent with Bragg scattering theory, where VV backscatter is always larger than  
15 HH. The  $PR_x$  is also inversely related to  $U_{10}$  and, above the  $3 \text{ ms}^{-1}$  threshold, varies by as much as 7–13 dB depending on the incidence angle. The negative trend is attributed to the enhanced sensitivity of HH to  $U_{10}$  compared to HV. The HV is sensitive to depolarised energy of which very little is expected to occur from wind-waves.

20 We conducted analysis of variance (ANOVA) F-statistic tests which showed that, for each of the bivariate relationships in Fig. 8, the slope of a linear regression line is significant ( $\neq 0$ ) when the  $U_{10} > 3 \text{ ms}^{-1}$ . On the other hand, the same test conducted on data from a  $\varphi = 90^\circ$  radar configuration (not shown) indicated no functional relationships between incidence angle and the polarisation ratios.

### 4.2.3 Upwind to crosswind ratios

25 Incidence angle dependent upwind to crosswind PR and  $PR_x$  are shown for three cases, named A–C in Fig. 9. Also shown in the figure are the corresponding wave amplitude profiles, their calculated  $s_w$ , and coincident  $U_{10}$  for each case. The lower incidence angle limit of  $35^\circ$  was chosen since it represents the approximate limit for the

Sea ice melt pond fraction estimation – Part 1

R. K. Scharien et al.

Title Page

Abstract

Introduction

Conclusions

References

Tables

Figures



Back

Close

Full Screen / Esc

Printer-friendly Version

Interactive Discussion



Bragg-like separation of VV and HH. The upper limit of  $50^\circ$  was chosen since some of the backscatter intensities from the smoothest case used in the calculation of PR and  $PR_x$  were below the system NESZ at larger incidence angles. Upwind to crosswind PR are close to unity for the two smoothest  $s_w$  cases, with the exception of case A at  $35^\circ$  which has an upwind to crosswind ratio of  $\sim 3$  dB. The roughest case, which is case C, has an upwind to crosswind PR of 3–4 dB at all incidence angles.  $PR_x$  upwind to crosswind ratios are greater than  $\sim 6$  dB for all cases.

Evaluating the Bragg limit  $ks$  yields a range of 0.14 to 0.49 for the three cases. Case B is the only case below the Bragg limit, case A is in proximity to the limit, and C is above it. This indicates a transition from Bragg to non-Bragg scattering across the three cases that is also consistent with the emergence of the observed PR dependency on  $\varphi$ . The emergence of this effect is undesirable from a satellite sensing perspective, since determining the relative contributions of  $\varphi$  and PR from spatially variable mixtures (pond fractions) would become very challenging. It is noteworthy that the highest recorded  $s_w$  in Fig. 9 did not coincide with the highest  $U_{10}$ , which further emphasizes the contribution of factors other than wind speed to pond roughness.

## 5 Discussion

Backscatter from undeformed FY ice is normally low, especially at large incidence angles. During the ponding season the possibility of calm ponds, combined with high pond fractions, exacerbates the possibility of noise floor contamination from low signal returns (De Abreu et al., 2001). Assessments of polarisation ratios must also consider the intensities of corresponding single-polarisation channels relative to noise levels. Until now our focus has been primarily on ponds; bare ice VV, HH, and HV intensities are shown in Fig. 10. VV and HH from bare ice are  $\geq -16$  dB across conventional satellite incidence angles ranges, and several dB above the worst case NESZ of SARs ENVISAT-ASAR and RS-2 (Scheuchl et al., 2004). When considered as an imaged mixture, i.e. in combination with pond measurements as shown in Fig. 7, the possibility

### Sea ice melt pond fraction estimation – Part 1

R. K. Scharien et al.

Title Page

Abstract

Introduction

Conclusions

References

Tables

Figures



Back

Close

Full Screen / Esc

Printer-friendly Version

Interactive Discussion





photo in Fig. 2. When the Bragg limit is exceeded, the surface roughness influence on PR, combined with the radar azimuth effect, would severely limit the interpretation of PR. Though we outlined the pond depth as variable affecting backscatter from ponds (Fig. 1) on the basis of a previous in situ scatterometer study (Scharien et al., 2012), no relationship was found here. This is likely due to the shallow (and limited range of) observed pond depths (0.03–0.08 m), resulting in no conclusive evidence of a pond depth influence on PR.

Using longer wavelengths extends the Bragg limit and potentially overcomes the pond surface roughness limitations outlined for C-band. Evaluating the Bragg limit using the maximum observed pond  $s_w$  (0.0066 m), while considering the  $k$  for lower frequency L- and P-band radars, yields  $ks$  values of 0.18 and 0.06, respectively. These values are below the Bragg limit of 0.3, suggesting longer wavelength missions such as PALSAR-2 (L-band) and the future BIOMASS (P-band) SAR may hold utility for Bragg based pond retrievals.

Finally, the formation of an ice lid on pond surfaces leads to a reduction in PR to levels similar to FY ice. This negates retrievals requiring response based on the permittivity contrast between pond and ice. As these events are more likely to occur during the overnight period, acquisition of associated SAR passes is undesirable in this context. Conversely, measured reductions in PR would enable the identification of freeze related events, provided a priori information of the existence of ponding is present. The freezing-melting state of sea ice is a key cryosphere variable with observational need, particularly in marginal ice zones (IGOS, 2007).

## 6 Conclusions

A study aimed at understanding the multiscale, polarimetric, C-band backscatter behaviour of FY ice during advanced melt for improved melt pond information retrievals was conducted in the Canadian Arctic Archipelago in June 2012. In situ polarimetric scatterometer data were collected along with surface roughness measurements of

TCD

8, 805–844, 2014

### Sea ice melt pond fraction estimation – Part 1

R. K. Scharien et al.

Title Page

Abstract

Introduction

Conclusions

References

Tables

Figures

⏪

⏩

◀

▶

Back

Close

Full Screen / Esc

Printer-friendly Version

Interactive Discussion



snow covered ice during melt onset, and bare ice and melt ponds during the ponding period. Coincident aerial photographs of pond covered ice were collected along with polarimetric backscatter data from the RADARSAT-2 satellite.

The following research questions were addressed: (1) do bare ice and melt ponds conform to the frequency-dependent surface roughness criterion of the Bragg scattering model? And (2) what are the limiting radar and target parameters on the unambiguous retrieval of melt pond information from dual-polarisation SAR? The ice surface during ponding conforms to the smooth-surface limit at C-band frequency, though melt pond roughness exceeded the limit when wind-waves of high amplitude were present on pond surfaces. Pond morphology must be considered together with wind speed as contributing to pond roughness and limiting PR retrievals. The primary limiting radar parameter is the incidence angle, as angles greater than about  $40^\circ$  are required in order to exploit the dielectric contrast between free water and ice. The orientation of the radar relative to wind-waves becomes a limiting factor on PR only when the Bragg limit is exceeded. These results suggest the limited utility of  $PR_x$  for unambiguous satellite retrievals of melt pond information due to noise floor contamination of HV intensity returns, combined with strong sensitivity (several dB) to the radar orientation relative to wind waves.

This study demonstrates the potential for SAR based PR approaches for monitoring melt pond parameters such as formation, evolution of pond fraction, and drainage. When pond surface roughness is below the Bragg limit, the retrieval of pond information on undeformed ice is achievable using the PR from dual-polarisation SAR. This is without the need for ancillary information. The dielectric contrast between the free surface water and FY ice cover types is sufficient to cause a detectable perturbation in the polarisation ratio (PR) at incidence angles above around  $40^\circ$ . The PR magnitude is independent of wind speed and direction, and by extension the radar azimuth direction, over the same incidence angle range. Data were evaluated at the in situ scale, which is of high spatial and temporal resolution compared to the outlined observation problem. Results at this scale are first necessary for understanding the complexities related to

## Sea ice melt pond fraction estimation – Part 1

R. K. Scharien et al.

Title Page

Abstract

Introduction

Conclusions

References

Tables

Figures

⏪

⏩

◀

▶

Back

Close

Full Screen / Esc

Printer-friendly Version

Interactive Discussion



radar and target parameters. They also provide a foundation for the utilization of future SAR missions. For example, future missions operating in constellation mode, such as ESA Sentinel-1 and Canada's Radarsat Constellation Mission (RCM), will provide high frequency coverage over polar regions. Applications requiring limited incidence angle ranges or specific polarisations, such as presented here, will be made possible. In part 2 of this study, the Bragg based PR approach will be extended to the satellite SAR scale, and melt pond fraction retrieval methods evaluated from RADARSAT-2 image data.

*Acknowledgements.* This paper is dedicated to our colleague Klaus Hochheim, who lost his life in September 2013, while conducting sea ice research in the Canadian Arctic. Funding for this research was in part provided by Natural Sciences and Engineering Research Council of Canada (NSERC), the Canada Research Chairs and Canada Excellence Research Chairs programs. Randall Scharien is the recipient of a European Space Agency Changing Earth Science Network postdoctoral fellowship for the period 2013–2015. Special thanks to John Yackel and his students Chris Fuller, J. V. Gill, and Carina Butterworth at the University of Calgary, for use of their polarimetric scatterometer. We acknowledge C. J. Mundy and all participants of Arctic-ICE 2012 for providing assistance and support in the field. Special thanks to the Polar Continental Shelf Project (PCSP) for logistical support during the field campaign.

## References

- Andreas, E. L., Persson, P. O. G., Jordan, R. E., Horst, T. W., Guest, P. S., Grachev, A. A., and Fairall, C. W.: Parameterizing the turbulent surface fluxes over summer sea ice, 8th Conf. on Polar Meteor. and Oceanog., 9–13 January 2005, San Diego, CA, Abstract 83848, 2005.
- Barber, D. G. and Yackel, J. J.: The physical, radiative and microwave scattering characteristics of melt ponds on Arctic landfast sea ice, *Int. J. Remote Sens.*, 20, 2069–2090, doi:10.1080/014311699212353, 1999.
- Barber, D. G., Papakyriakou, T. N., LeDrew, E. F., and Shokr, M. E.: An examination of the relation between the spring period evolution of the scattering coefficient ( $\sigma^\circ$ ) and radiative fluxes over landfast sea-ice, *Int. J. Remote Sens.*, 16, 3343–3363, 1995.

## Sea ice melt pond fraction estimation – Part 1

R. K. Scharien et al.

Title Page

Abstract

Introduction

Conclusions

References

Tables

Figures

◀

▶

◀

▶

Back

Close

Full Screen / Esc

Printer-friendly Version

Interactive Discussion



---

**Sea ice melt pond  
fraction estimation –  
Part 1**R. K. Scharien et al.

---

[Title Page](#)[Abstract](#)[Introduction](#)[Conclusions](#)[References](#)[Tables](#)[Figures](#)[◀](#)[▶](#)[◀](#)[▶](#)[Back](#)[Close](#)[Full Screen / Esc](#)[Printer-friendly Version](#)[Interactive Discussion](#)

Belchansky, G. I., Douglas, D. C., Eremeev, V. A., and Platonov, N. G.: Variations in the Arctic's multiyear sea ice cover: a neural network analysis of SMMR-SSM/I data, 1979–2004, *Geophys. Res. Lett.*, 32, L09605, doi:10.1029/2005GL022395, 2005.

Brekke, C., Holt, B., Jones, C., and Skrunes, S.: Towards oil slick monitoring in the Arctic environment, *Proc. POLinSAR 2013*, Frascati, Italy, 28 January–1 February 2013, 8, 2013.

Donelan, M. A. and Pierson Jr., W. J.: Radar scattering and equilibrium ranges in wind-generated waves with application to scatterometry, *J. Geophys. Res.*, 92, 4971–5029, doi:10.1029/JC092iC05p04971, 1987.

Eicken, H., Krouse, H. R., Kadko, D., and Perovich, D. K.: Tracer studies of pathways and rates of meltwater transport through Arctic summer sea ice, *J. Geophys. Res.*, 107, 8046, doi:10.1029/2000JC000583, 2002.

Eicken, H., Grenfell, T. C., Perovich, D. K., Richter-Menge, J. A., and Frey, K.: Hydraulic controls on summer Arctic pack ice albedo, *J. Geophys. Res.*, 109, C08007, doi:10.1029/2003JC001989, 2004.

Fung, A. K.: *Microwave Scattering and Emission Models and Their Applications*, Artech House, Inc., Norwood, Ma., 1994.

Geldsetzer, T. and Yackel, J. J.: Sea ice type and open water discrimination using dual co-polarized C-band SAR, *Can. J. Remote Sens.*, 35, 73–84, doi:10.5589/m08-075, 2009.

Geldsetzer, T., Mead, J. B., Yackel, J. J., Scharien, R. K., and Howell, S. E. L.: Surface-based polarimetric C-band scatterometer for field measurements of sea ice, *IEEE T. Geosci. Remote*, 45, 3405–3416, 2007.

Hallikainen, M. T. and Winebrenner, D. P.: The physical basis for sea ice remote sensing, in: *Microwave Remote Sensing of Sea Ice*, Geophysical Monograph 68, edited by: Carsey, F., AGU, Washington, DC, 29–46, 1992.

Hajsek, I., Pottier, E., and Cloude, S. R.: Inversion of surface parameters from polarimetric SAR, *IEEE T. Geosci. Remote*, 41, 727–744, 2003.

Hanesiak, J. M., Yackel, J. J., and Barber, D. G.: Effect of melt ponds on first-year sea ice ablation-integration of RADARSAT-1 and thermodynamic modelling, *Can. J. Remote Sens.*, 27, 433–442, 2001.

Heygster, G., Alexandrov, V., Dybkjær, G., von Hoyningen-Huene, W., Girard-Ardhuin, F., Katsev, I. L., Kokhanovsky, A., Lavergne, T., Malinka, A. V., Melsheimer, C., Toudal Pedersen, L., Prikhach, A. S., Saldo, R., Tonboe, R., Wiebe, H., and Zege, E. P.: Remote sensing of sea ice:

---

**Sea ice melt pond  
fraction estimation –  
Part 1**R. K. Scharien et al.

---

[Title Page](#)[Abstract](#)[Introduction](#)[Conclusions](#)[References](#)[Tables](#)[Figures](#)[◀](#)[▶](#)[◀](#)[▶](#)[Back](#)[Close](#)[Full Screen / Esc](#)[Printer-friendly Version](#)[Interactive Discussion](#)

advances during the DAMOCLES project, *The Cryosphere*, 6, 1411–1434, doi:10.5194/tc-6-1411-2012, 2012.

Holland, M. M., Bailey, D. A., Briegleb, B. P., Light, B., and Hunke, E.: Improved sea ice short-wave radiation physics in ccs4: the impact of melt ponds and aerosols on arctic sea ice, *J. Climate*, 25, 1413–1430, doi:10.1175/JCLI-D-11-00078.1, 2012.

Horstmann, J., Kock, W., Lehner, S., and Tonboe, R.: Wind retrieval over the ocean using synthetic aperture radar with C-band HH polarization, *IEEE T. Geosci. Remote*, 38, 2122–2131, doi:10.1109/36.868871, 2000.

Howell, S. E. L., Tivy, A., Yackel, J. J., and Scharien, R. K.: Application of a SeaWinds/QuikSCAT sea ice melt algorithm for assessing melt dynamics in the Canadian Arctic Archipelago, *J. Geophys. Res.*, 111, C07025, doi:10.1029/2005JC003193, 2006.

IGOS Cryosphere: Integrated Global Observing Strategy (IGOS) cryosphere theme report, WMO/TD-No. 1405, Geneva, Switzerland, 102 pp., 2007.

Kwok, R., Cunningham, G. F., Wensnahan, M., Rigor, I., Zwally, H. J., and Yi, D.: Thinning and volume loss of the Arctic Ocean sea ice cover: 2003–2008, *J. Geophys. Res.*, 114, C07005, doi:10.1029/2009JC005312, 2009.

Landy, J. C., Isleifson, D., and Barber, D. G.: Parameterization of sea ice surface roughness using LiDAR, in review, 2014.

Livingstone, C. E., Singh, K.P. and Gray, L.: Seasonal and regional variations of active/passive microwave signatures of sea ice, *IEEE T. Geosci. Remote*, 25, 159–187, 1987.

Markus, T., Cavalieri, D. J., Tschudi, M. A., and Ivanoff, A.: Comparison of aerial video and Landsat 7 data over ponded sea ice, *Remote Sens. Environ.*, 86, 458–469, 2003.

Morassutti, M. P. and Ledrew, E. F.: Albedo and depth of melt ponds on sea ice, *Int. J. Climatol.*, 16, 817–838, doi:10.1002/(SICI)1097-0088(199607)16:7<817::AID-JOC44>3.0.CO;2-5, 1996.

Nakamura, K., Wakabayashi, H., Uto, S., Ushio, S., and Nishio, F.: Observation of sea-ice thickness using ENVISAT data from Lützow-Holm Bay, East Antarctica, *IEEE Geosci. Remote S.*, 6, 277–281, doi:10.1109/LGRS.2008.2011061, 2009.

Nghiem, S. V. and Bertoia, C.: Study of multi-polarization C-band backscatter signatures for Arctic sea ice mapping with future satellite SAR, *Can. J. Remote Sens.*, 27, 387–402, 2001.

Perovich, D. K., Grenfell, T. C., Richter-Menge, J. A., Light, B., Tucker III, W. B., and Eicken, H.: Thin and thinner: sea ice mass balance measurements during SHEBA, *J. Geophys. Res.*, 108, 8050, doi:10.1029/2001JC001079, 2003.

## Sea ice melt pond fraction estimation – Part 1

R. K. Scharien et al.

Title Page

Abstract

Introduction

Conclusions

References

Tables

Figures

◀

▶

◀

▶

Back

Close

Full Screen / Esc

Printer-friendly Version

Interactive Discussion



- Perovich, D. K., Light, B., Eicken, H., Jones, K. F., Runciman, K., and Nghiem, S. V.: Increasing solar heating of the Arctic Ocean and adjacent seas, 1979–2005: attribution and role in the ice-albedo feedback, *Geophys. Res. Lett.*, 34, L19505, doi:10.1029/2007GL031480, 2007.
- Plant, W. J.: Bragg Scattering of Electromagnetic Waves from the Air/Sea Interface, in: *Surface Waves and Fluxes: Current Theory and Remote Sensing*, edited by: Geernaert, G. L. and Plant, W. J., Kluwer Academic Publishers, Dordrecht, The Netherlands, 2, 41–108, 1990.
- Polashenski, C., Perovich, D., and Courville, Z.: The mechanisms of sea ice melt pond formation and evolution, *J. Geophys. Res.*, 117, C01001, doi:10.1029/2011JC007231, 2012.
- Rösel, A. and Kaleschke, L.: Comparison of different retrieval techniques for melt ponds on Arctic sea ice from Landsat and MODIS satellite data, *Ann. Glaciol.*, 52, 185–191, 2011.
- Rösel, A. and Kaleschke, L.: Exceptional melt pond occurrence in the years 2007 and 2011 on the Arctic sea ice revealed from MODIS satellite data, *J. Geophys. Res.*, 117, C05018, doi:10.1029/2011JC007869, 2012.
- Rösel, A., Kaleschke, L., and Birnbaum, G.: Melt ponds on Arctic sea ice determined from MODIS satellite data using an artificial neural network, *The Cryosphere*, 6, 431–446, doi:10.5194/tc-6-431-2012, 2012.
- Scharien, R. K. and Yackel, J. J.: Analysis of surface roughness and morphology of first-year sea ice melt ponds: implications for microwave scattering, *IEEE T. Geosci. Remote Sens.*, 43, 2927–2939, 2005.
- Scharien, R. K., Geldsetzer, T., Barber, D. G., Yackel, J. J., and Langlois, A.: Physical, dielectric, and C band microwave scattering properties of first-year sea ice during advanced melt, *J. Geophys. Res.*, 115, C12026, doi:10.1029/2010JC006257, 2010.
- Scharien, R. K., Yackel, J. J., Barber, D. G., Asplin, M., Gupta, M., and Isleifson, D.: Geophysical controls on C band polarimetric backscatter from melt pond covered Arctic first-year sea ice: Assessment using high-resolution scatterometry, *J. Geophys. Res.*, 117, C00G18, doi:10.1029/2011JC007353, 2012.
- Thomsen, B. B., Nghiem, S. V., and Kwok, R.: Polarimetric C-band SAR observations of sea ice in the Greenland Sea, *Proc. Int. Geoscience and Remote Sensing Symp.*, Seattle, WA, 6–10 July 1998, 2502–2504, doi:10.1109/IGARSS.1998.702259, 1998.
- Thompson, D., Elfouhaily, T., and Chapron, B.: Polarization ratio for microwave backscattering from the ocean surface at low to moderate incidence angles, *Proc. Int. Geoscience and Remote Sensing Symp.*, Seattle, WA, 6–10 July 1998, 1671–1673, doi:10.1109/IGARSS.1998.692411, 1998.

## Sea ice melt pond fraction estimation – Part 1

R. K. Scharien et al.

Title Page

Abstract

Introduction

Conclusions

References

Tables

Figures

◀

▶

◀

▶

Back

Close

Full Screen / Esc

Printer-friendly Version

Interactive Discussion



- Tschudi, M. A., Maslanik, J. A., and Perovich, D. K.: Derivation of melt pond coverage on Arctic sea ice using MODIS observations, *Remote Sens. Environ.*, 112, 2605–2614, 2008.
- Ulaby, F. T., Moore, R. K., and Fung, A. K.: *Microwave Remote Sensing: Active and Passive, From Theory to Applications*, Vol. III, Artech House, Inc., Norwood, Massachusetts, 1986.
- 5 Untersteiner, N.: Arctic Summer Time: The Short Summer of 2004, available at: [http://www.arctic.noaa.gov/essay\\_untersteiner3.html](http://www.arctic.noaa.gov/essay_untersteiner3.html) (15 November 2013), 2004.
- Vachon, P. W. and Wolfe, J.: C-Band cross-polarization wind speed retrieval, *Geosci. Remote Sens. Lett.*, 8, 451–455, doi:10.1109/LGRS.2010.2085417, 2011.
- Yackel, J. J. and Barber, D. G.: Melt ponds on sea ice in the Canadian Archipelago 2. on the use of RADARSAT-1 synthetic aperture radar for geophysical inversion, *J. Geophys. Res.-Oceans*, 105, 22061–22069, 2000.
- 10 Yackel, J. J., Barber, D. G., Papakyriakou, T. N., and Breneman, C.: First-year sea ice spring melt transitions in the Canadian Arctic Archipelago from time-series synthetic aperture radar data, 1992–2002, *Hydrol. Process.*, 21, 253–265, doi:10.1002/hyp.6240, 2007.
- 15 Zabel, I., Jezek, K., Gogineni, S., and Kanagaratnam, P.: Search for proxy indicators of young sea ice thickness, *J. Geophys. Res.*, 101, 6697–6709, doi:10.1029/95JC02957, 1996.
- Zege, E., Katsev, I., Malinka, A., Prikhach, A., and Heygster, G.: New approach for radiative transfer in sea ice and its application for sea ice satellite remote sensing, *Radiation Processes in the Atmosphere and Ocean (IRS2012)*, AIP Conf. Proc. 1531, 43–46, doi:10.1063/1.4804703, 2012.
- 20 Zhang, B., Perrie, W., and He, Y.: Wind speed retrieval from RADARSAT-2 quad-polarization images using a new polarization ratio model, *J. Geophys. Res.*, 116, C08008, doi:10.1029/2010JC006522, 2011.

## Sea ice melt pond fraction estimation – Part 1

R. K. Scharien et al.

**Table 1.** Cscat radar parameters.

Parameter	Specification
Frequency	5.5 GHz (C-band)
Antenna Beam Width	5.4°
Bandwidth	5–500 MHz
Range Resolution	0.30 m
Polarisation	HH + HV + VH + VV
Noise Floor	Co-polarised: –35 dB Cross-polarised: –45 dB
Incidence Angle	25° –65° (5° interval)
Azimuth Width	Ice: 40° Melt pond: 20°
External Calibration	Trihedral Corner Reflector

Title Page

Abstract

Introduction

Conclusions

References

Tables

Figures

◀

▶

◀

▶

Back

Close

Full Screen / Esc

Printer-friendly Version

Interactive Discussion



## TCD

8, 805–844, 2014

Sea ice melt pond  
fraction estimation –  
Part 1

R. K. Scharien et al.

Title Page

Abstract

Introduction

Conclusions

References

Tables

Figures

◀

▶

◀

▶

Back

Close

Full Screen / Esc

Printer-friendly Version

Interactive Discussion

**Table 2.** PR (dB) model coefficients for a melt pond.

Model	A	B	C
PR Cscat	1.320	−0.103	0.004

## Sea ice melt pond fraction estimation – Part 1

R. K. Scharien et al.

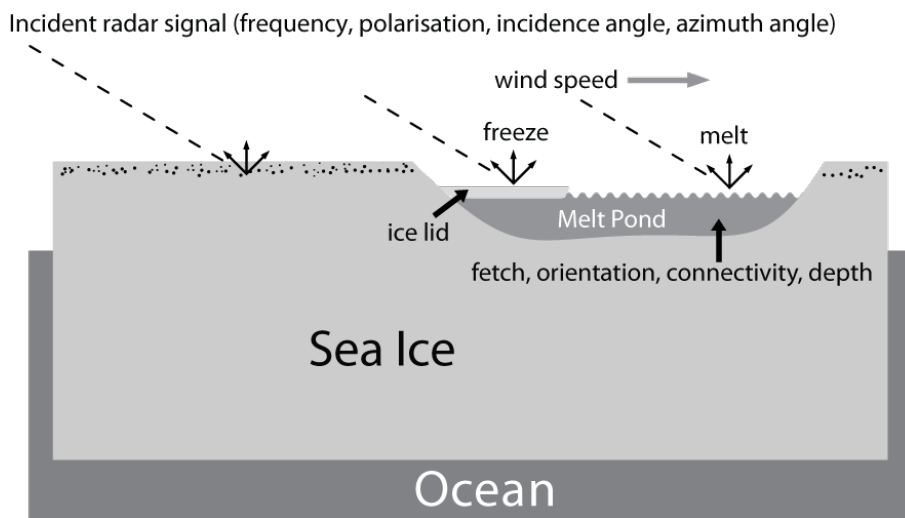


**Fig. 1.** Schematization of the radar and target parameters under consideration for the in situ study of backscatter from first-year sea ice melt ponds.

Title Page

Abstract

Introduction

Conclusions

References

Tables

Figures

◀

▶

◀

▶

Back

Close

Full Screen / Esc

Printer-friendly Version

Interactive Discussion



## Sea ice melt pond fraction estimation – Part 1

R. K. Scharien et al.

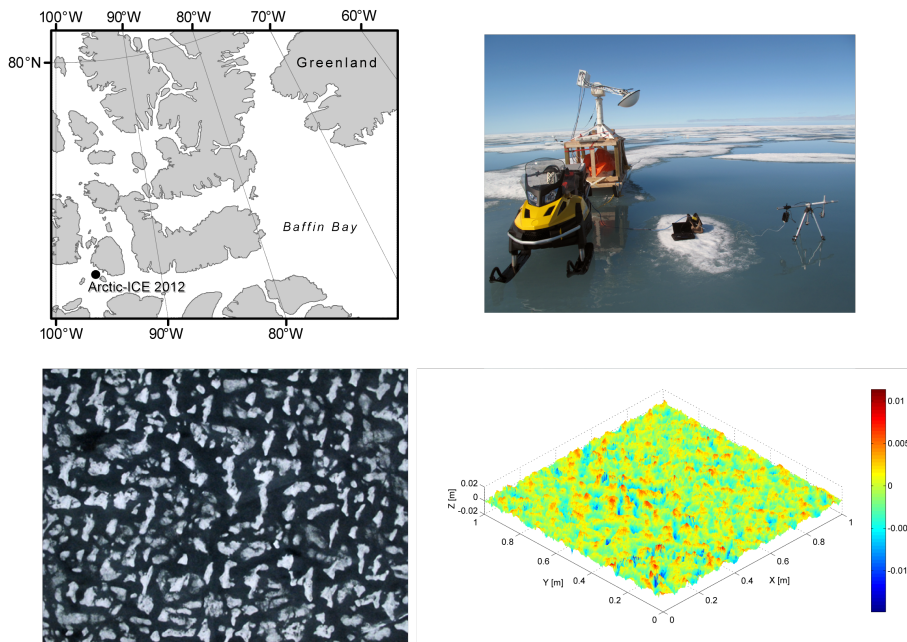


**Fig. 2.** (Left, top) Map of field site. (Right, top) Oblique photo of Cscat set up for a melt pond scan, with tripod-mounted ultrasonic sensor in the pond. (Right, bottom) Exemplative small-scale surface elevation map of bare ice. (Left, bottom) Aerial photo taken over field study site on 24 June 2012. The photo was taken at 210 m altitude and covers a 250 m wide swath.

[Title Page](#)[Abstract](#)[Introduction](#)[Conclusions](#)[References](#)[Tables](#)[Figures](#)[◀](#)[▶](#)[◀](#)[▶](#)[Back](#)[Close](#)[Full Screen / Esc](#)[Printer-friendly Version](#)[Interactive Discussion](#)

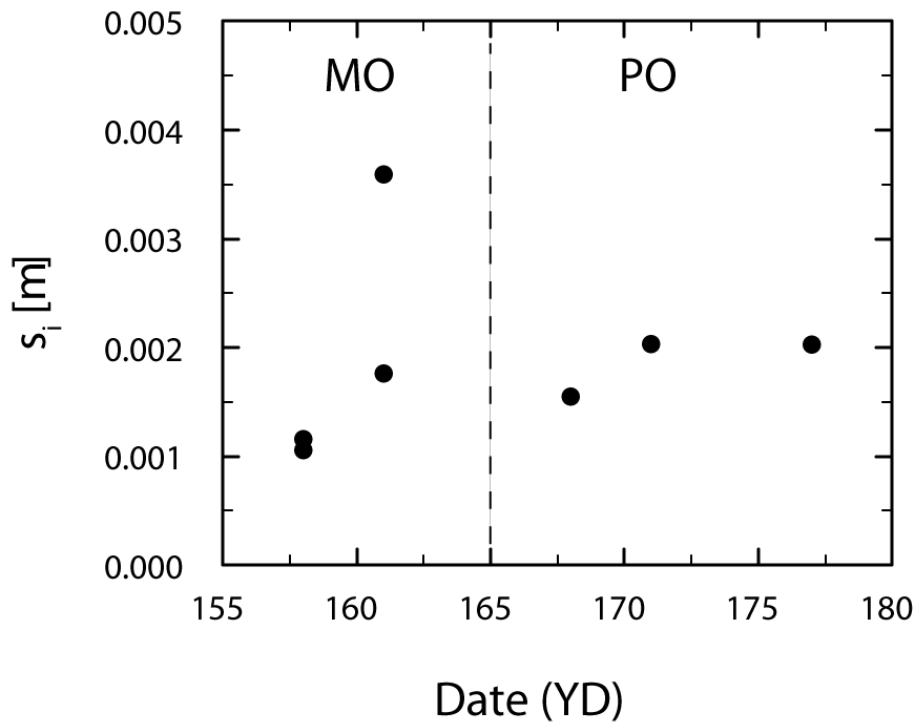


**Fig. 3.** Surface roughness parameter  $s_i$ , taken during melt onset (MO) and during ponding (PO). The onset of the ponding period is denoted by vertical line.

Sea ice melt pond fraction estimation – Part 1

R. K. Scharien et al.

Title Page

Abstract

Introduction

Conclusions

References

Tables

Figures

◀

▶

◀

▶

Back

Close

Full Screen / Esc

Printer-friendly Version

Interactive Discussion



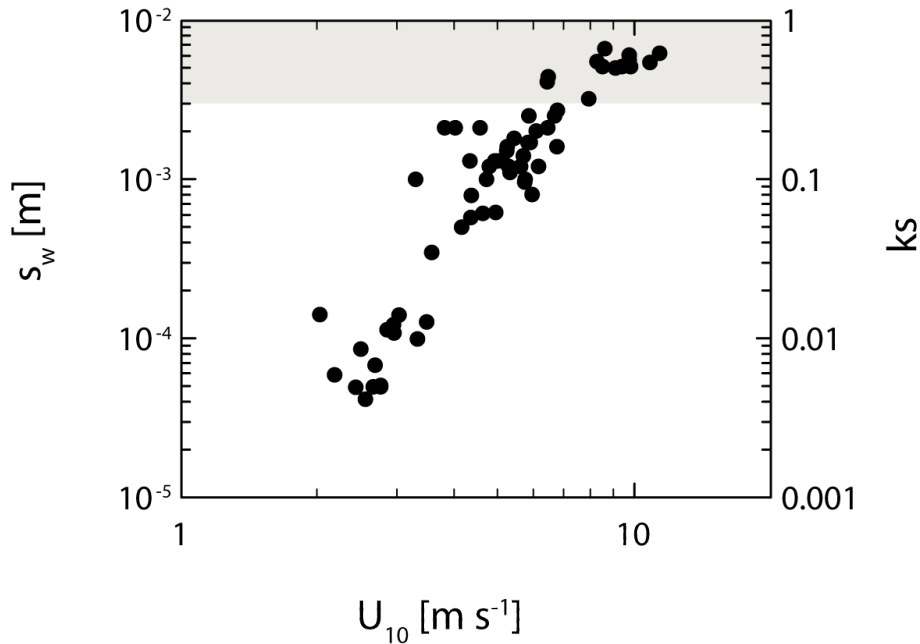


**Fig. 4.** Log-log plot of melt pond surface roughness parameters  $s_w$  (left-axis) and  $ks$  evaluated at the C-band frequency radar wavenumber (right-axis) against wind speed  $U_{10}$ . The shaded portion denotes the area within which  $ks$  values exceed the roughness limit of the Bragg model.

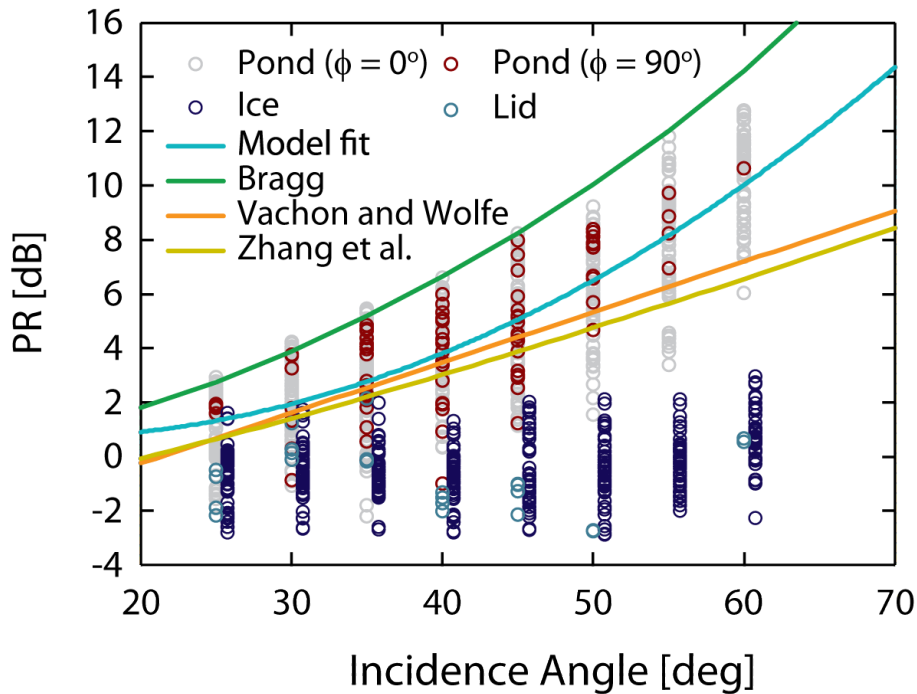


**Fig. 5.** Cscat measured polarisation ratio PR (VV/HH) vs. incidence angle and azimuth angle ( $\phi$ ), from surface types pond, frozen pond (lid), and ice. Note that the ice observations are off-set along the x-axis by  $1^\circ$  for clarity. Solid lines correspond to a fits to pond data, the Bragg scattering model estimate for ponds, and ocean PR model estimates, as discussed in the text.

Sea ice melt pond fraction estimation – Part 1

R. K. Scharien et al.

Title Page

Abstract Introduction

Conclusions References

Tables Figures

◀ ▶

◀ ▶

Back Close

Full Screen / Esc

Printer-friendly Version

Interactive Discussion



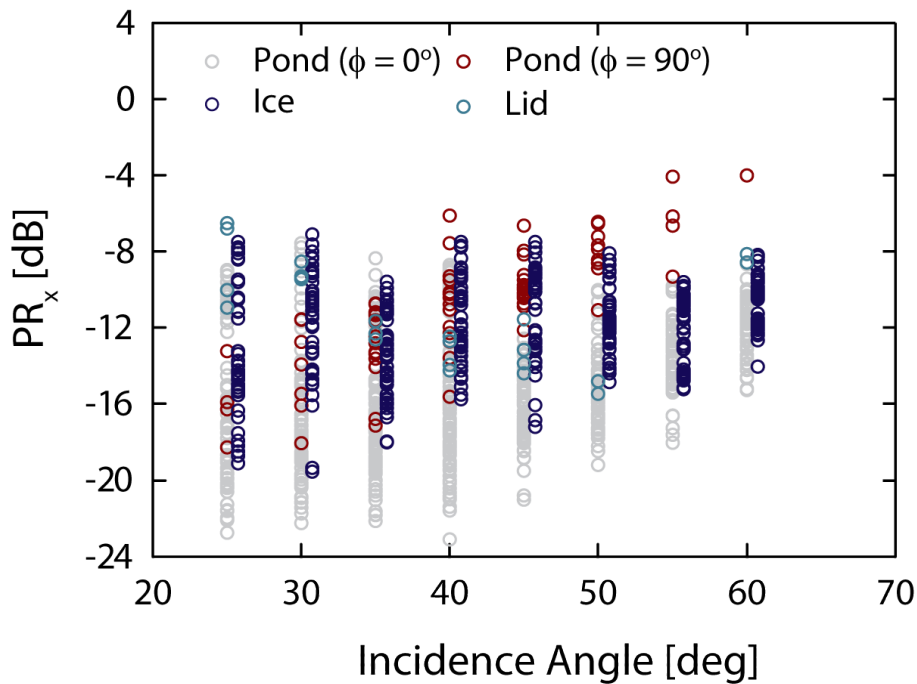


**Fig. 6.** Same as in Fig. 5, but for the polarisation ratio  $PR_x$  (HV/HH).

Title Page

Abstract Introduction

Conclusions References

Tables Figures

◀ ▶

◀ ▶

Back Close

Full Screen / Esc

Printer-friendly Version

Interactive Discussion



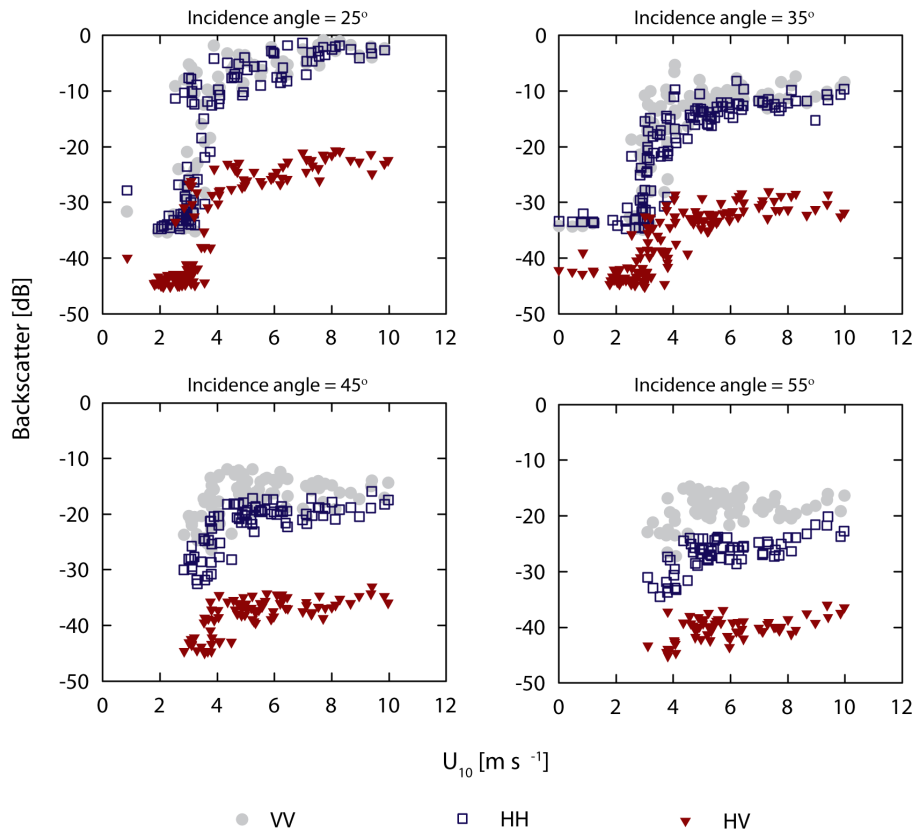


**Fig. 7.** Linear VV, HH, and HV polarisation backscatter vs. wind speed  $U_{10}$ , at  $10^\circ$  incidence angle intervals from  $25^\circ$  to  $55^\circ$ . All samples were taken with  $\varphi = 0^\circ$ .

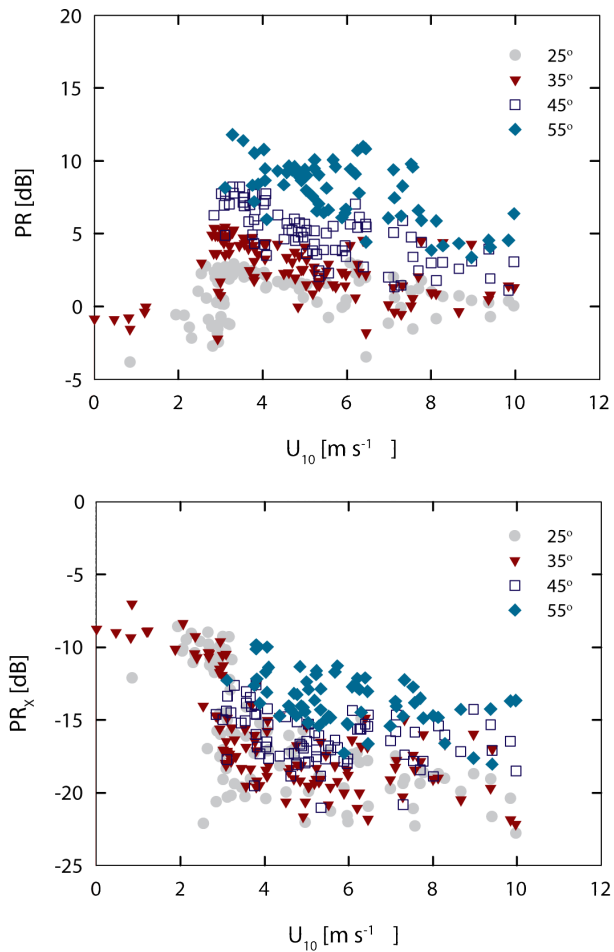


**Fig. 8.** Polarisation ratios PR and  $PR_x$  vs. wind speed  $U_{10}$  at  $10^\circ$  incidence angle intervals from  $25^\circ$  to  $55^\circ$ . All samples were taken with  $\varphi = 0^\circ$ .

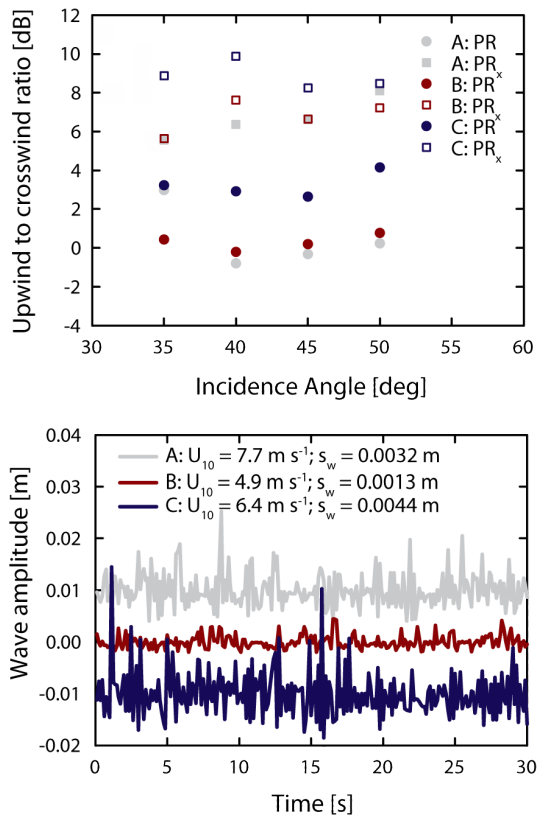


**Fig. 9.** (Top) Incidence angle dependent upwind-to-crosswind PR and PR<sub>x</sub> for cases A–C. (Bottom) Surface wave amplitude profiles for cases A–C, offset along the y-axis for clarity. Also shown in the bottom figure are coincident wind speed  $U_{10}$  and pond roughness  $s_w$  derived from each amplitude profile.

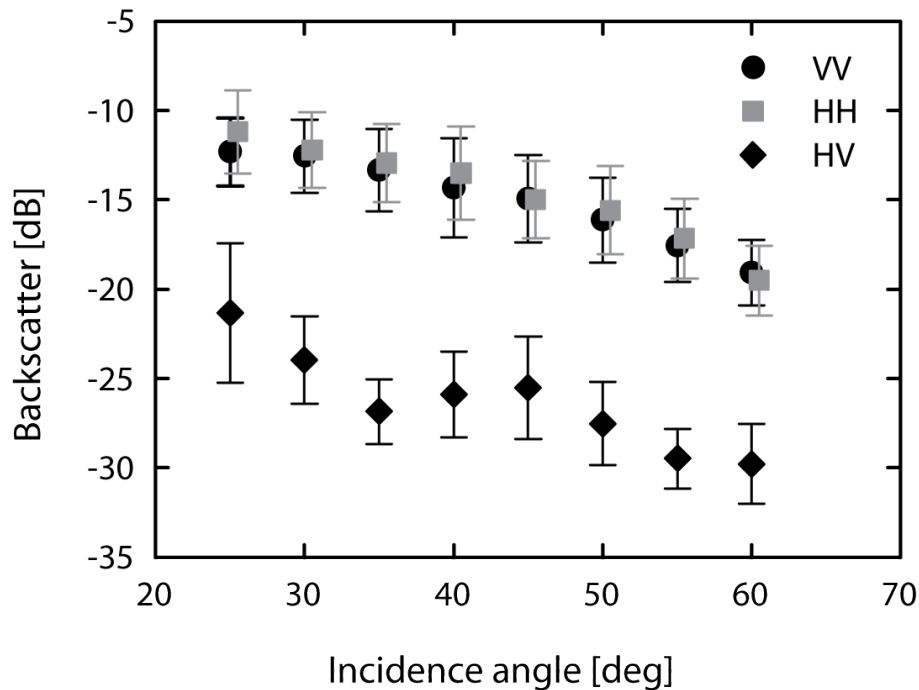


**Fig. 10.** Linear VV, HH, and HV polarisation backscatter vs. incidence angle, for the ice cover adjacent to ponds.

**Sea ice melt pond fraction estimation – Part 1**

R. K. Scharien et al.

[Title Page](#)

[Abstract](#) | [Introduction](#)

[Conclusions](#) | [References](#)

[Tables](#) | [Figures](#)

[◀](#) | [▶](#)

[◀](#) | [▶](#)

[Back](#) | [Close](#)

[Full Screen / Esc](#)

[Printer-friendly Version](#)

[Interactive Discussion](#)

